EES Batteries

Accepted Manuscript

This article can be cited before page numbers have been issued, to do this please use: M. Radi, D. Tchitchekova, A. Ponrouch and R. Dedryvère, *EES Batteries*, 2026, DOI: 10.1039/D6EB00065G.

View Article Online
DOI: 10.1039/D6EB00065G

Concerns about the long-term sustainability, costs, and resource limitations linked to lithium-ion technology have led the battery research community to focus on developing alternative energy storage options. Among these, rechargeable magnesium batteries (RMBs) are emerging as a promising choice due to their reliance on an abundant earth metal. Magnesium not only offers a high volumetric capacity, but magnesium metal anodes are also inherently safer than lithium metal ones, because they are less prone to forming dendrites. These merits make RMBs attractive for large-scale energy storage. However, progress is obstructed by the lack of suitable electrolytes that enable reversible magnesium plating and stripping. Most standard electrolytes form passivation layers that block Mg^{2+} ion transport, causing significant voltage hysteresis and low coulombic efficiency.

Therefore, innovative strategies such as electrode interphase engineering and electrolyte optimization should be utilized for advancing RMBs. This study investigates the effect of specific additives on the $Mg(TFSI)_2$/DME:DG electrolyte system. Especially, we find that BI_3 additive promotes significantly the RMBs' performance, which is explained by the formation of a thin interphase that is rich in boron and iodine. This research offers valuable insights into interphase engineering for improving the performance of RMBs.

View Article Online
DOI: 10.1039/D6EB00065G

Electrode surface engineering with electrolyte additives, improving reversibility of magnesium metal anode batteries

Muath Radi[1]*, Deyana S. Tchitchekova[2], Alexandre Ponrouch[2]* and Rémi Dedryvère[1,3]*

[1] IPREM, Université de Pau & Pays Adour, CNRS UMR 5254, E2S-UPPA, 64000, Pau, France

[2] Institut de Ciencia de Materials de Barcelona, ICMAB-CSIC, Campus UAB, 08193, Bellaterra, Spain

[3] RS2E, Réseau sur le Stockage Electrochimique de l'Energie, FR CNRS 3459, France

* E-mail: muath-m-m.radi@univ-pau.fr, remi.dedryvere@univ-pau.fr, aponrouch@icmab.es.

Abstract

Rechargeable magnesium batteries (RMBs) are promising energy storage systems because of magnesium's high volumetric capacity and abundance. However, RMBs' advancement has been hindered by the lack of suitable electrolytes that combine high oxidative stability and electrodes compatibility. In this study, we investigate the effect of three mechanistically different additives, namely boron trifluoride diethyl etherate ($BF_3{\cdot}O(C_2H_5)_2$), iodine (I_2), and boron triiodide (BI_3) in $Mg(TFSI)_2$/DME:DG electrolyte, on magnesium plating and stripping kinetics, voltage hysteresis, coulombic efficiency, and modify the composition and thickness of the electrode interphase. BI_3 demonstrates the greatest beneficial effect among these additives by forming a thin (<5 nm) interphase, rich in iodide and boron species, that enhances the coulombic efficiency (from <60 to 80–90%), reduces voltage hysteresis (from 2000 mV to 250–350 mV), and improves Mg plating/stripping kinetics. Electrochemical tests against Mo_6S_8 cathodes demonstrate that substrate choice also affects performance: Mo_6S_8 supported on stainless steel yields stable cycling with full capacity retention, whereas titanium exhibits poor adhesion of the cathode composite material. Compared to state-of-the-art $Mg[B(HFIP)_4]_2$ electrolytes, $Mg(TFSI)_2$/DME:DG + BI_3 offers a simpler, more scalable, and practical route with engineered interphase chemistry, though further studies are needed to match the outstanding performance of $Mg[B(HFIP)_4]_2$, and to fully understand $Mg(TFSI)_2$/DME:DG + BI_3 bulk electrolyte properties. This work provides key insights for designing improved-performance RMBs via innovative interphase engineering and electrolyte formulation.

View Article Online
DOI: 10.1039/D6EB00065G

1) Introduction

Rechargeable magnesium batteries (RMBs) have received increasing attention in the energy storage field due to the unique properties of Mg metal, including high volumetric capacity, improved resistance to dendrite formation compared to other metals like lithium and high elemental abundance in the Earth's crust. The low redox potential of magnesium and its divalent charge carriers provide large theoretical energy densities, making Mg systems a promising alternative to Li-ion batteries. Nevertheless, efficient RMBs have been constrained by a key challenge: identifying suitable electrolytes that enable fully reversible Mg plating and stripping. A good electrolyte must also have high oxidative stability, compatibility with the two electrodes, and be less expensive in terms of raw materials[1,2].

One promising approach is the use of magnesium salts with weakly coordinating anions, such as $TFSI^-$, which is commercially available, halide-free, and exhibits excellent solubility in aprotic ether solutions. These electrolytes typically provide high ionic conductivity and wide electrochemical windows[3,4]. Despite these advantages, $Mg(TFSI)_2$-based electrolytes still suffer from important limitations, such as electrolyte decomposition (both salt and solvent) and the reaction of trace moisture with the magnesium electrode, leading to surface passivation. These processes lead to significant plating/stripping overpotentials and reduced Coulombic efficiency, representing a serious obstacle for practical Mg batteries[5,6].

Recent studies increasingly suggest that the nature of the interphase formed on Mg metal plays a decisive role in determining plating/stripping reversibility. Additive strategies have therefore been developed to (i) scavenge impurities, (ii) alter Mg^{2+} solvation, or (iii) engineer the interphase chemistry as summarized in Table S1. For example, impurity-scavenging additives such as heptamethyldisilazane (HpMS)[7] or dibutyl magnesium ($Mg(butyl)_2$)[5] improve performance by mitigating hydroxide formation, effectively removing trace water from the electrolytes and modifying the surface chemistry. Solvation-modifying agents, including crown ethers[8,9] or diamines[10] improve the electrochemical performance of $Mg(TFSI)_2$-based electrolytes by altering Mg^{2+} coordination and reducing solvent/anion reduction. Co-salt strategies using $Mg(BH_4)_2$ have also been proposed to suppress $TFSI^-$ reduction via preferential anion adsorption[11].

A more recent approach involves engineering a solid electrolyte interphase (SEI) on Mg surface. This strategy was historically considered challenging because stable interphases often

hinder Mg^{2+} transport.[12] However, it was reported that adding 50 mM I_2 to a 0.5 M $Mg(TFSI)_2$ / DME electrolyte significantly decreases the voltage hysteresis between Mg plating and stripping from 2.67 V to 0.22 V. This improvement was attributed to the formation of a Mg-ion conducting surface layer containing magnesium iodide (MgI_2), confirmed by XPS analysis[13]. In addition, for state-of-the-art Mg electrolytes based on alkoxyborate anions, boron-containing surface layers have been identified as beneficial interphase components enabling efficient Mg plating/stripping[14]. Although the passivation layer formed on Mg metal is rarely characterized in detail and remains poorly understood, it is becoming increasingly evident that Mg metal negative electrodes can operate effectively in the presence of such passivation layers.

Similarly, boron-containing species have been identified as key components of functional interphases in other multivalent systems. For example in calcium batteries, BF_3·DE based-electrolyte additives have been shown to promote reversible Ca plating by forming ion-conductive boron-containing interphases.

Despite these advances, a systematic comparison between boron-derived interphases (from BF_3·DE Lewis acid), iodide-derived interphases (from I_2 chemistry), and their combined effects within the same $Mg(TFSI)_2$–glyme electrolyte has not yet been reported. More broadly, it remains unclear whether boron-based strategies successfully applied in Ca systems can be effectively translated to Mg electrolytes, and how their effects compare directly with iodine-derived surface modification.

In this work, we address this gap by investigating three mechanistically different additives in 0.4 M $Mg(TFSI)_2$ in DME/DG (1:1 wt.%):

- **BF_3·DE**, a strong Lewis acid selected to modify Mg^{2+} solvation, promote the formation of boron-containing interphases and scavenge electrolyte impurities;
- **I_2**, a halogen additive known to form MgI_2 surface layers and improve Mg reversibility;
- **BI_3**, a hybrid additive combining Lewis acidity with the in situ formation of boron and iodide species in the electrode interphase.

All the additives are evaluated within the same electrolyte to allow a direct comparison of their effects. In addition, their concentrations are varied across low, medium, and high regimes to identify the optimal range for interphase engineering without affecting bulk electrolyte properties.

View Article Online
DOI: 10.1039/D6EB00065G

The effects on Mg plating/stripping behavior, voltage hysteresis, Coulombic efficiency, and interphase composition are examined using electrochemical measurements, SEM, and XPS. The compatibility of the optimized electrolyte formulation with the Mo_6S_8 Chevrel phase cathode is also evaluated.

In summary, this study proposes a stepwise strategy for engineering the Mg electrode interphase through selected electrolyte additives to improve Mg plating/stripping reversibility and overall battery performance. It systematically compares boron-based, iodine-based, and combined-function additives in $Mg(TFSI)_2$ glyme electrolytes, highlighting how each chemistry regulates the interphase formulation and correlates it to the Mg plating/stripping reversibility.

2) Experimental Section/Methods

Electrolyte preparation:

The additives, including Boron trifluoride diethyl etherate (BF_3·DE, >46.5% BF_3, Sigma Aldrich), Iodine flakes (I_2, ReagentPlus®, ≥99%) and boron triiodide (BI_3, 95 % Sigma Aldrich), were added to an electrolyte solution. The electrolyte was composed of 0.4 M $Mg(TFSI)_2$, (99.5% purity, Solvionic) dissolved in a 50/50 wt.% mixture of DME (Sigma-Aldrich, anhydrous, 99.0%) and DG (Sigma-Aldrich, anhydrous, 99.7%).

BF_3·DE was added at 1.5, 4, and 8 wt.% while I_2 and BI_3 were added at 10, 20, and 40 mM. These concentrations were selected based on previous studies, [13,15] aiming to ensure that these additives, especially I_2 and BI_3 primarily influence the electrode interphase composition rather than altering the bulk solvation structure of the electrolyte, and limits the chemical reactivity with Mg metal electrodes.

The $Mg(TFSI)_2$ salt was dried under vacuum for 12 h at 90°C. The solvents were dried over molecular sieves (3 Å from Alfa Aesar) for a minimum of 2 days. The water content of the electrolyte before adding the additives was below 15 ppm as measured by Karl Fischer titrations inside an argon-filled glove box. A lower water content is expected after adding the BF_3 and BI_3, but measuring the water content by Karl Fischer is unsuitable after adding these species due to their reactivity. A total of 400 µL of electrolyte was used in each cell.

Chevrel phase electrode preparation:

Chevrel phase (Mo_6S_8) powder was purchased from NEI Corp., USA. The slurry was prepared by mixing the active material with carbon black (Super P, Timcal, Switzerland) and

View Article Online
DOI: 10.1039/D6EB00065G

polyvinylidene fluoride (PVDF, Arkema) in a weight ratio of 80:10:10, and the mixture was dispersed in N-methyl-2-pyrrolidone (NMP, Aldrich, ≥99.9%). The slurry was then cast using a doctor blade onto 10 µm thick stainless steel (SS, Goodfellow, AISI 316) and titanium (Ti, Goodfellow, 99.6%) foils, and vacuum-dried at 80°C for 20 hours. Disc electrodes were punched at a 10 mm diameter, and the active mass loading was around 2-3 mg/cm^2 for Mo_6S_8 electrodes on SS and around 3-4 mg/cm^2 on Ti.

Electrochemical measurements:

T-shape 3-electrode Swagelok cells were assembled with a Ti disk (Goodfellow, 99.6%) punched at Ø10 mm as the working electrode (WE), a magnesium disk (Mateck, 99.98%) as the counter electrode, and a silver wire (Sigma Aldrich) as a quasi-reference electrode (Ag_{QRE}). Cellulose separators were used. All cells were assembled inside an argon-filled glovebox with O_2 and H_2O concentrations below 1 ppm, and electrochemical tests were performed using a Bio-Logic VSP300 potentiostat. The electrochemical protocol for Mg plating/stripping includes three consecutive steps: (1) The cells were connected at open circuit voltage (OCV) for 2h. (2) Galvanostatic Cycling with Potential Limitation (GCPL) was applied as a conditioning step for 50 cycles at 0.1 mA/cm^2 with two constraints: potential limitation - 4 to 2 V *vs.* Ag_{QRE} and 10 minutes for each half cycle. (3) The cells were cycled between 0.4 and - 3.0 V *vs.* Ag_{QRE} with a scan rate of 25 mV/s with -5 mA as a current limitation at reduction using a Modular Potentio (MP) technique. The coulombic efficiency was calculated based on the following equations:

$$C.E. = \frac{Q_{stripping}}{|Q_{plating}|} \times 100\%$$

$$\text{where } Q = \int_{t1}^{t2} I\,(t)\,dt$$

For anodic stability tests, linear sweep voltammetry (LSV) at 0.1 mV/s was performed on SS, Ti and Al working electrodes. The anodic stability was estimated when the oxidation current reached 0.1 mA/cm^2. The electrochemical testing of the Mo_6S_8 cathode was performed with GCPL at C/10 in a 2-electrode Swagelok cell using a Mg disc counter electrode.

X-Ray Photoelectron Spectroscopy analysis:

The cells were disassembled inside an argon-filled glovebox, and the recovered electrodes were washed with dry DME before being dried inside the glovebox for a few hours. A Thermo Scientific ESCALAB 250 spectrometer was used, which is equipped with an argon-filled glove box, to maintain the samples under an inert atmosphere during all times of preparation for their

View Article Online
DOI: 10.1039/D6EB00065G

analysis. XPS measurements were performed with a focused monochromatized Al Kα radiation ($h\nu$ = 1486.6 eV), and the spectra were recorded with a pass energy of 20 eV and 600 µm spot size. The analysis was done using the standard charge compensation, and the analysis chamber pressure was maintained around 2×10^{-7} mbar during the flood gun operation. The binding energy scale was calibrated using the C 1s peak at 285 eV associated with adventitious hydrocarbon. The data were fitted and analysed using CasaXPS software with the relative sensitivity factor (RSF) of the ESCALAB database.

Scanning Electron Microscopy (SEM):

The SEM images were recorded with a JEOL JAMP 9500F Auger spectrometer (JEOL Ltd, Tokyo, Japan) working under UHV and fitted with a Schottky field emission electron gun, using a conventional secondary electron detector (SED) in the analysis chamber. The following conditions were applied: 20 keV, working distance 22-23 mm, with –30 degrees of specimen tilt angle. For SEM images of BI_3 additive sample, FEI Quanta 650 FEG microscope under high vacuum operating at 20 kV and 9.9 mm working distance was used, and the Energy Dispersive spectroscopy (EDS) analysis was done with an Inca 250 SSD XMax20 detector.

3) Results and Discussion

a) BF_3·DE additive

Figure 1(a) displays the cyclic voltammetry (CV) of a Ti WE with 0.4 M $Mg(TFSI)_2$ in DME:DG electrolyte. Upon cycling, the oxidation peak broadens and steadily shifts to higher potential values, leading to a loss of charge related to Mg stripping and the accumulation of metallic Mg on the substrate surface. In contrast, the onset potential for plating and the plating kinetics (i.e. slope of the reduction wave) remain constant throughout cycling. Noticeably, the voltage hysteresis between plating and stripping is higher than 2 V.

Figure 1(b) illustrates the impact of adding 1.5 wt.% BF_3·DE to the 0.4 M $Mg(TFSI)_2$ electrolyte. In the first cycle, a residual reduction current was observed before plating, possibly indicating contributions from capacitive currents (ion adsorption on the electrode) and/or partial electrolyte decomposition. Notably, during the plating process, a nucleation loop is present, where the reverse current scan (anodic) is larger than the forward current scan (cathodic), as indicated by a curved arrow. Additionally, the oxidation process (stripping) occurs with two peaks, one small and sharp peak at about -1.75 V *vs.* Ag_{QRE} (peak A) and another much broader peak appears above -1.25 V *vs.* Ag_{QRE} (peak B). Peak A appears only during the initial cycles

View Article Online
DOI: 10.1039/D6EB00065G

and disappears after 30 cycles, which indicates changes in the electrode surface or in the electrolyte composition over cycling.

Figures 1(c) and (d) depict similar patterns with the addition of 4 wt.% and 8 wt.% BF_3·DE, respectively. Both figures also show two oxidation peaks (A and B), although the potential difference between them diminishes with higher additive concentrations. Unlike the 1.5 wt.% case, both oxidation peaks consistently appear in all cycles with 4 wt.% BF_3·DE. For 8 wt.%, stripping peaks only become apparent after a few cycles. Notably, in Figures 1(c) and (d), the first cycle does not exhibit the nucleation loop during plating, and a significant reduction current is recorded at a potential as high as -1 V *vs.* Ag_{QRE}, suggesting non-negligible electrolyte reduction, affecting the nucleation process. For the two electrolytes containing 4 and 8 wt.% BF_3·DE, a small reduction peak appears before the main reduction wave (peak C).

Lastly, Figure 1(e) compares the 30th cycle for the different BF_3·DE concentrations (0 wt.%, 1.5 wt.%, 4 wt.%, and 8 wt.%). Higher concentrations of BF_3·DE lead to a lower voltage hysteresis between plating and stripping, the lowest (*ca.* 600 mV) being recorded with 8 wt.% BF_3·DE, which shows also the lowest onset potential for the stripping peak B, recorded at –1.25 V *vs.* $Ag_{QRE,}$ compared with 0, -0.6 and -1.0 V *vs.* Ag_{QRE} for 0, 1.5 and 4 wt.% BF_3·DE, respectively. However, adding BF_3·DE does not improve the coulombic efficiency (at cycle 30, ~60% with 1.5 wt.% BF_3·DE, ~30% with 4 wt.% and ~27% with 8 wt.% BF_3·DE comparing with ~52% with 0 wt.% BF_3·DE) or the kinetics of plating/stripping. Indeed, across all BF_3·DE concentrations, the stripping peak B remains broad, indicating slow kinetics of the stripping process.

Due to its lower voltage hysteresis between Mg plating and stripping processes, the deposit obtained with 8 wt.% BF_3·DE is selected for Mg deposition experiment, which was achieved using potentiostatic deposition for one hour at –2.26 V *vs.* Ag_{QRE} (potential corresponding to the maximum current of the reduction wave), after 30 cyclic voltammetry (CV) cycles (see Figure S1 in the supporting information).

View Article Online
DOI: 10.1039/D6EB00065G

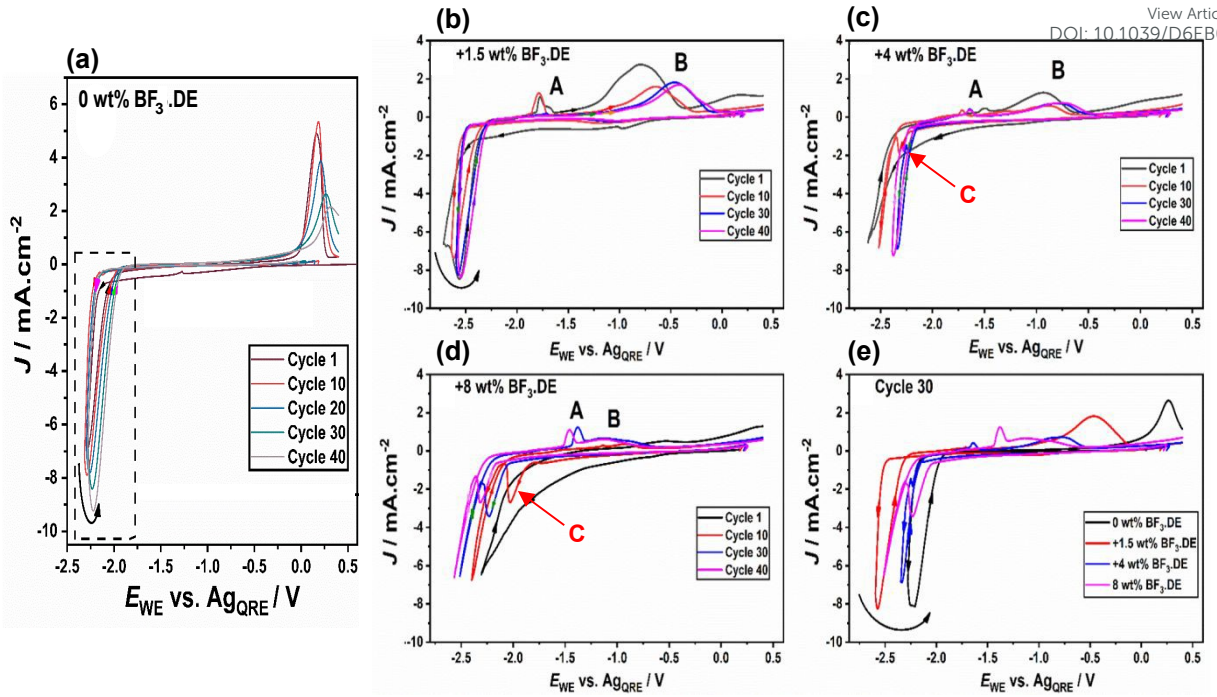

Figure 1: Cyclic voltammograms (25 mV/s) of a Ti WE electrode using (a) 0.4 M $Mg(TFSI)_2$ in DME:DG electrolyte (adapted from ref. [5], licensed under the terms of the CC BY-NC 4.0) and after adding (b) 1.5 wt.%, (c) 4 wt.%, (d) 8 wt.% BF_3·DE. (e) Comparison of the 30th CV cycle with different wt.% of BF_3·DE additive.

To understand the impact of the BF_3·DE additive on the chemical composition of the electrode interphase, XPS analysis was performed on the samples prepared from the electrolyte containing different wt.% of BF_3·DE at the end of the 50th plating scan, previously shown in Figures 1 and S1, and the results are presented in Figure 2. C 1s spectra in Figure 2 (a-d) can be fitted with three components, indicating the presence of carbon atoms in CH_x, CO, and COO groups, accompanied by a weak fourth peak associated to CO_3 environments, which is mainly attributed to the presence of $MgCO_3$ in the sample after one hour of potentiostatic deposition (Figure 2(d)). Table S2 lists the atomic percentages for each element with the chemical attributions of each XPS component. From this quantification table, we deduce the estimated atomic percentages of some identified chemical species. To do so, the contributions of all atoms participating in the composition of one species are considered (e.g., at.% $MgCO_3$ = at.% Mg + at.% C + at.% O, which is equivalent to 5 × at.% C_{CO_3}). These calculated atomic percentages of the identified chemical species are shown in the stacked bar in Chart 1. The S 2p spectra show sulfur in three environments: the highest E_B component corresponds to the TFSI salt, while very

View Article Online
DOI: 10.1039/D6EB00065G

small blue and red components around 167.5 eV and 161.5 eV suggest degradation products of the salt and formation of sulfite and MgS, respectively.

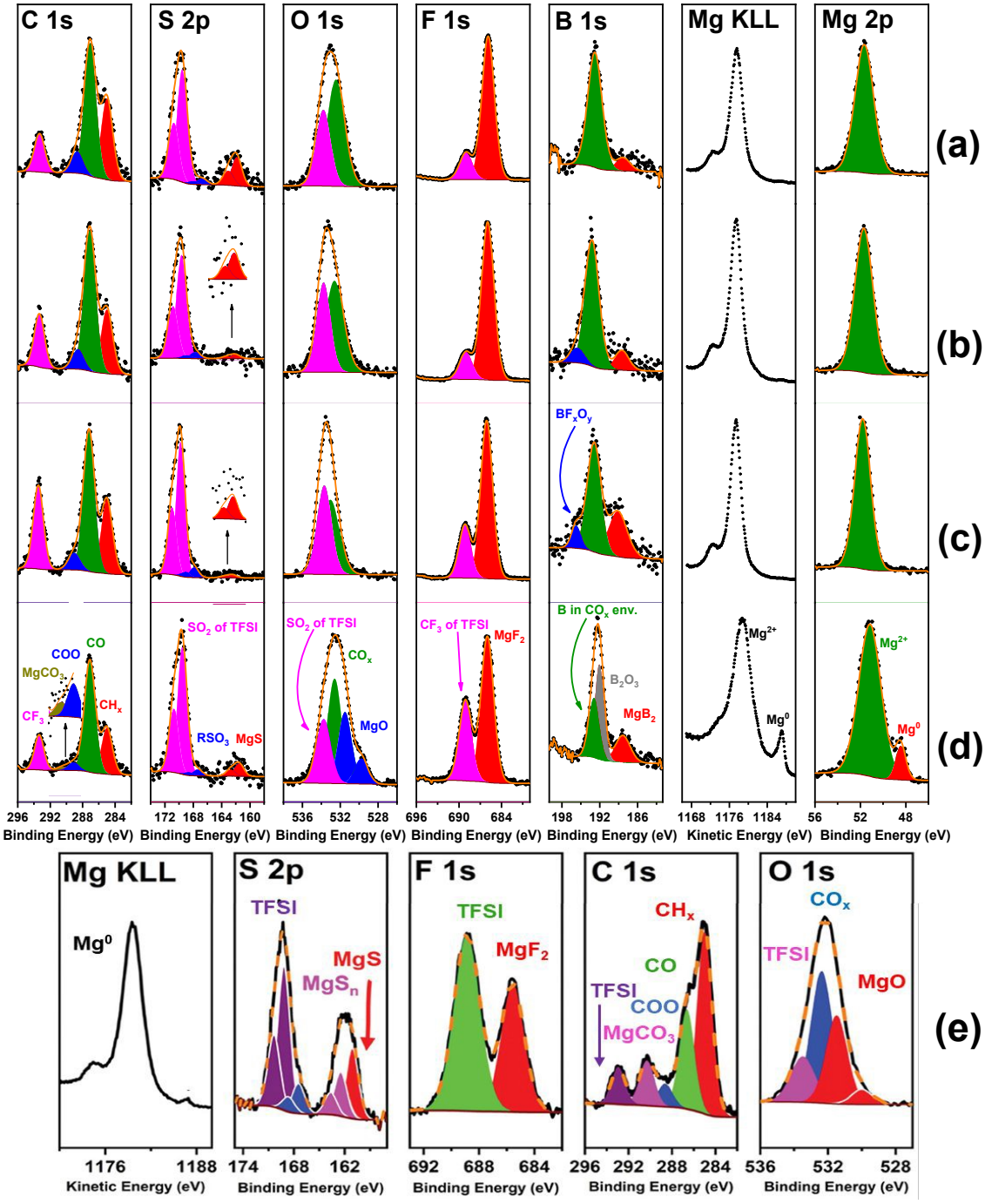

Figure 2: (a-d) XPS C 1s, S 2p, O 1s, F 1s, B 1s and Mg 2p and Auger Mg KLL spectra of the electrode interphase formed on Ti electrode cycled in the electrolyte with adding (a) 1.5 wt.% BF_3.DE, (b) 4 wt.% BF_3.DE, (c) 8 wt.% BF_3.DE at the end of 50th plating scan (see Figure 1), and (d) after 30th stripping scan followed by 1 hour of Mg potentiostatic deposition (PSD) at – 2.26 V vs. Ag_{QRE} with 8 wt.% BF_3.DE electrolytes (see Figure S1). (e) Mg KLL Auger and XPS S 2p, F 1s, C 1s and O 1s spectra of the interphase formed on Ti electrode cycled in 0.4

View Article Online
DOI: 10.1039/D6EB00065G

M $Mg(TFSI)_2$ in DME:DG electrolyte without additive (adapted from ref. [5], licensed under the terms of the CC BY-NC 4.0).

The O 1s spectrum indicates the presence of organic oxygen (CO_x) and the oxygen from TFSI salt in Figure 2 (a-c). However, in Figure 2 (d), after 1 hour of the potentiostatic deposition, there is a significant amount of MgO (~19 at.%), likely related to the presence of metallic Mg clearly detected in the Mg 2p and Mg KLL spectra. This suggests that during one hour of potentiostatic deposition, metallic Mg accumulates and can be detected by XPS, whereas potentiodynamic deposition via CV is insufficient to detect the deposited Mg. Note that the O 1s signal of MgO is split into two components due to the differential charging effect, as we already discussed in our previous work [5,16].

Theoretically, assuming 100% plating efficiency and a homogeneous surface distribution, the charge associated with the reduction waves in Figure 1d (~150–68 mC) would yield a 139–63 nm thick Mg film, which is sufficient for XPS detection. This calculation is done considering the Faraday equation:

$$d = \frac{Q.M}{\mathrm{n}F\rho A}$$

Where:

d : thickness of deposited Mg (cm)

Q : total charge passed during plating (C)

M : molar mass of Mg (24.305 g mol^{-1})

n : number of electrons per Mg atom (2 for Mg^{2+})

F : Faraday constant (96485 C mol^{-1})

ρ : density of Mg (1.738 g cm^{-3})

A : electrode surface area (0.785 cm^2)

These results suggest that (i) a significant portion of the plating charge is consumed by the interphase formation and electrolyte decomposition rather than metallic Mg growth, and/or (ii) Mg deposition is highly inhomogeneous.

View Article Online
DOI: 10.1039/D6EB00065G

The F 1s spectrum in the samples shows two peaks: one corresponding to MgF_2 at lower E_B and the other one associated to TFSI. In the samples after potentiodynamic deposition (CV, Figure 2 (a-c), MgF_2 is present in vast amounts (58, 63 and 54 at.%, respectively, see Table S2 and Chart 1). In contrast, only 9 and 27 at.% were measured, respectively, in potentiodynamic deposition without BF_3·DE and in potentiostatic mode with 8 wt.% BF_3.DE electrolytes, pointing at the addition of BF_3.DE and potentiodynamic deposition significantly favoring MgF_2 formation.

Upon adding BF_3·DE, the amounts of MgS and $MgCO_3$ decrease significantly. For example, MgS decreases from ~3 at.% without the additive to ~1 at.% with 1.5 wt.% BF_3·DE, and becomes nearly negligible at 4 wt.% and 8 wt.% BF_3·DE. Similarly, $MgCO_3$, initially accounting for 13 at.%, is no longer detectable after introducing BF_3·DE. These observations suggest that BF_3·DE appears to limit the salt degradation, and that most of the MgF_2 likely originates from BF_3·DE rather than from TFSI anion degradation. It has been found that the MgF_2 passivating layer suppresses side reactions with the electrolyte [17]. This observation leads to the conclusion that the large amount of MgF_2 on the electrode surface protects the TFSI salt from degradation, as evidenced by the absence of $TFSI^-$ degradation products in the S 2p spectrum. However, MgF_2 is not a suitable coating material for Mg anodes due to its high Mg migration barrier (~1123 meV) [18], which could explain the slow kinetics observed in the stripping process in Figure 1 (b-d).

The B 1s spectrum in Figure 2 (a) displays two peaks: the main peak in green corresponds to boron in an oxygen environment, and a lower binding energy peak in red is ascribed to MgB_2. A third peak in blue appears with more BF_3·DE addition (Figure 2 b and 2 c), due to partial degradation of BF_3·DE into BF_xO_y, while the main peak in green indicates that most of BF_3 is replaced by boron in an oxygen environment. Quantitative calculations reveal that all O 1s components in Figure 2 (a-c) correspond to organic oxygen (CO_x groups) and the salt's oxygen, leaving no remaining oxygen for inorganic boron oxygen species (B_xO_y). This means that the main B 1s peak is associated to boron bound to the organic oxygen (CO_x). In contrast, in the sample shown in Figure 2 (d), calculations of the remaining oxygen indicate that a portion of boron (2 at.%) exists in an inorganic oxygen environment, likely as B_2O_3 as estimated from the B/O ratio. It has been reported that a B-containing organic/inorganic SEI layer significantly enhances Mg ion diffusion at the interface and improves long-term cycling stability [14,19]. Therefore, the presence of boron in organic/inorganic environments in our sample likely explains the decreased voltage hysteresis observed in the Mg plating/stripping process when

View Article Online
DOI: 10.1039/D6EE00065G

BF_3·DE is added, as evidenced in Figure 1. Similarly, the BF_3·DE additive has proven beneficial effect on Ca plating, forming a boron cross-linked polymer in the electrode interphase and enhancing Ca^{2+} conductivity [20].

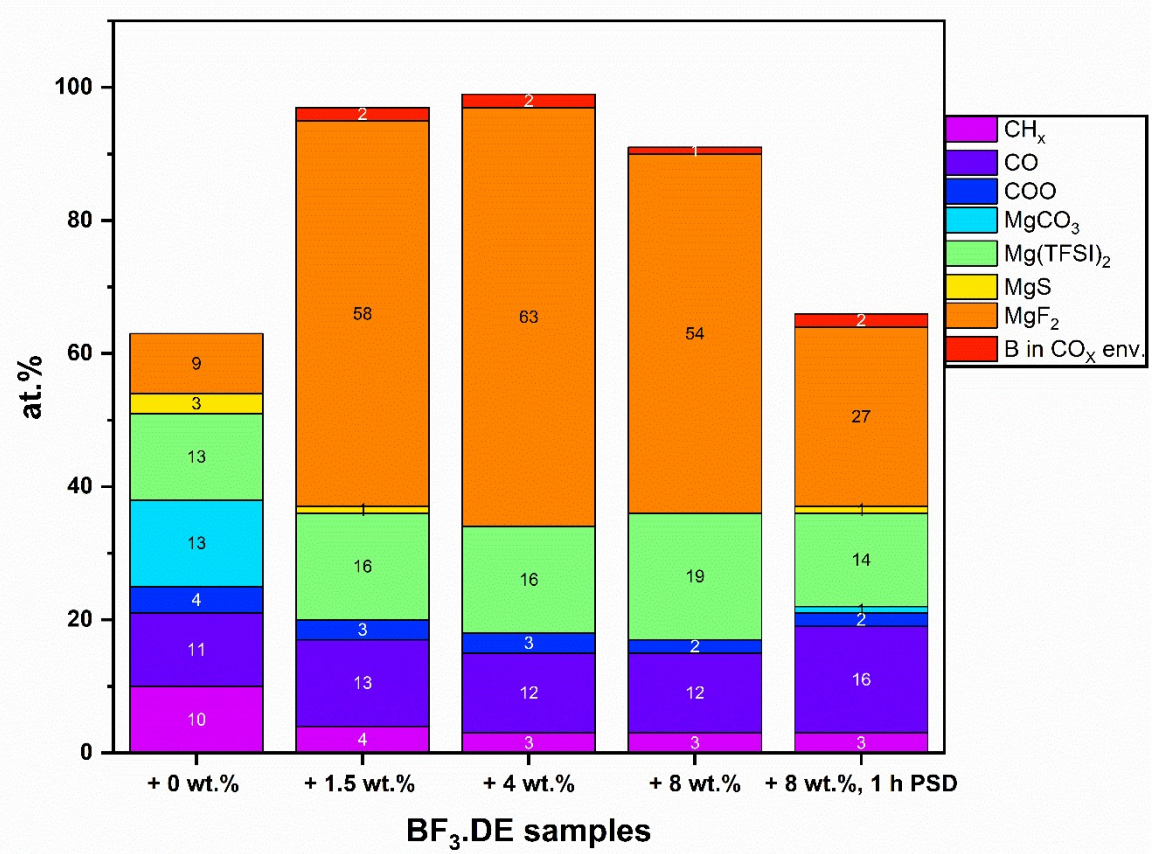

Chart 1: Atomic percentage (at.%) of some of the chemical species observed in XPS spectra reported in Figure 2 and Table S2 of the electrode interphase formed on Ti electrodes cycled in 0.4 M $Mg(TFSI)_2$ in DME:DG electrolyte with addition of different wt.% BF_3·DE.

Finally, the Ti substrate is not detectable in both samples (by its Ti 2p spectrum), indicating that the electrode interphase is thicker than the XPS analysis depth (> 5 nm) and fully covers the substrate. Therefore, although a slow Mg^{2+} solid-state diffusion is achieved, these results demonstrate the feasibility of Mg plating/stripping in the presence of a stable and conformal electrode interphase.

The morphology of the electrodes after a potentiostatic deposition with 8 wt.% BF_3·DE additive was examined using SEM (Figure S2). The Mg deposits do not uniformly cover the Ti substrate

View Article Online
DOI: 10.1039/D6EB00065G

but form a continuous film with multiple cracks and nearly spherical particles embedded within the film. But aside from the cracks, the deposit is rather smooth. These cracks may indicate a metallic characteristic of the deposit because of its internal mechanical stress, or can be the result of the fast drying of a deposit with solvent inclusions.

b) I_2 additive

Figure 3 illustrates the impact of adding different concentrations of iodine (10 mM, 20 mM and 40 mM) to a 0.4 M $Mg(TFSI)_2$ electrolyte over several cycles. In all cases, there is no significant effect on the plating peak, but two distinct oxidation peaks, labelled A and B, emerge after the addition of 10 mM and 20 mM of iodine. The first peak (A) occurs at a lower overpotential with voltage hysteresis of 500-680 mV and 400-650 mV for 10 mM and 20 mM, respectively. Peak (A) intensity increases as the concentration of iodine rises from 10 mM to 20 mM. After adding 40 mM of I_2, only one stripping peak occurs with very low voltage hysteresis between onset potentials of plating and stripping (~350mV), and the cyclic voltammograms appear to be quite stable except for a potential shift towards negative potential values of the entire CV curve, associated with an instability of the quasi-reference electrode. The coulombic efficiency is 70 % for the first cycle, then it increases to stabilize around 83% in the following cycles, as shown in the inset in Figure 3 (d). For the sake of comparison, the coulombic efficiency achieved at cycle 30 without I_2 is less than 50%. The dramatic improvement in terms of plating/stripping kinetics and coulombic efficiency when adding 40 mM iodine is illustrated in Figure 4 (d). The addition of iodine significantly reduces the voltage hysteresis (from 2000mV to 350mV). Adding more iodine to the electrolyte (+ 90 mM) does not result in improved coulombic efficiency, as shown in Figure S3.

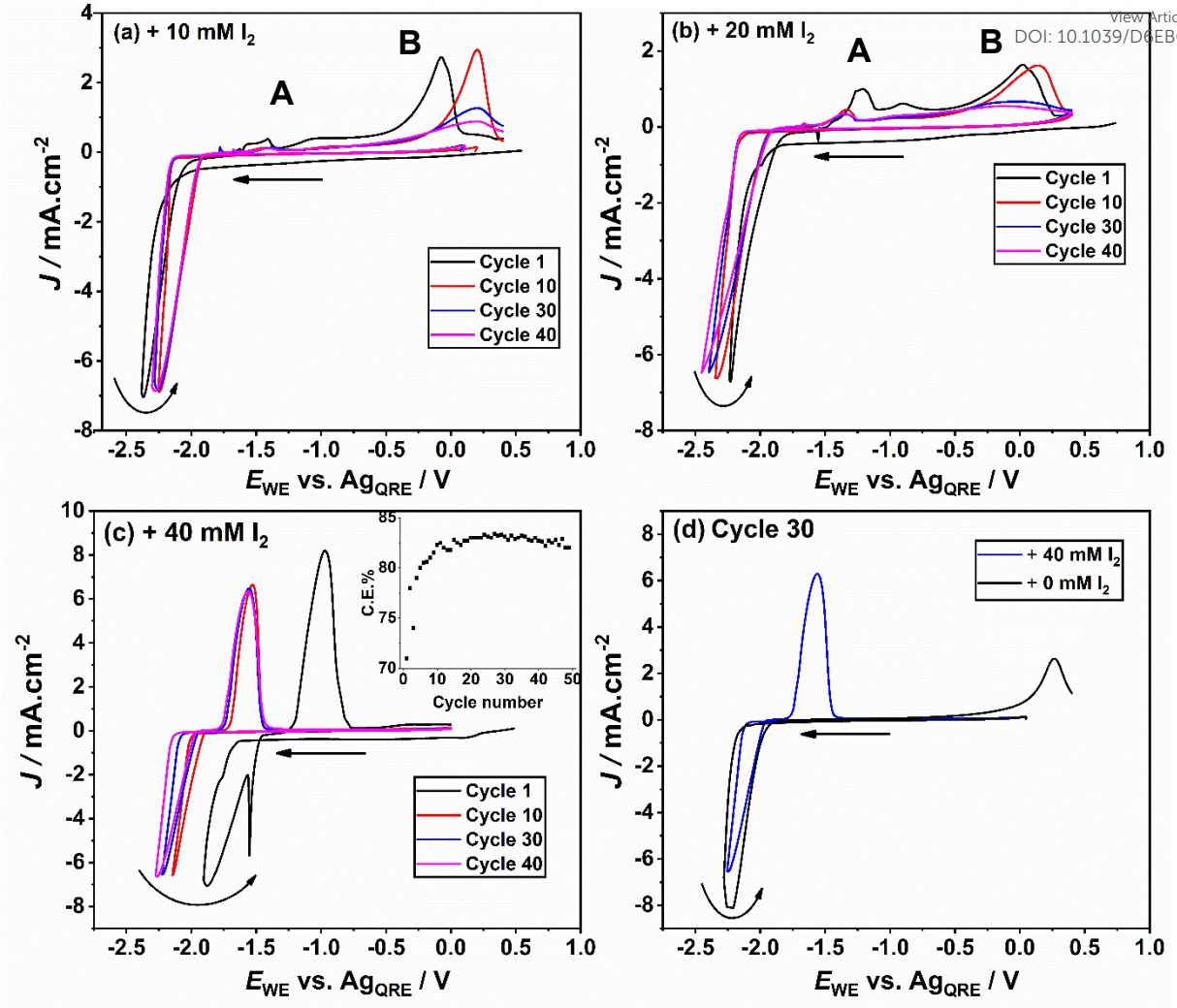

Figure 3: Cyclic voltammograms of a Ti electrode with a scan rate of 25 mV/s at several cycle numbers using 0.4 M $Mg(TFSI)_2$ in DME:DG electrolyte with adding (a) 10 mM, (b) 20 mM, (c) 40 mM of I_2 and (d) Comparison of the 30th CV cycle of 0.4 M $Mg(TFSI)_2$ electrolyte with and without the addition of 40 mM of I_2 additive. The inset shows the coulombic efficiency over the cycle number.

XPS measurement of the electrode interphase on the Ti electrode using 0.4 M $Mg(TFSI)_2$ electrolyte with the different concentrations of I_2, stopped at the end of the 50th plating scan, is shown in Figure 4. By utilizing the quantification data in Table S3 (Supporting Information), the atomic percentages of identified chemical species were calculated and summarized in Chart 2. C 1s spectra indicate that the surface of the electrode is covered by hydrocarbon (~285 eV), as well as organic components with C–O and COO groups, which are products of electrolyte degradation, particularly from the solvent. Additionally, a carbonate environment is observed,

View Article Online
DOI: 10.1039/D6EB00065G

likely due to $MgCO_3$, and CF_3 groups of the salt. The presence of MgS and MgF_2 detected in the S 2p and F 1s spectra, respectively, also indicates the salt degradation. The I $3d_{5/2}$ spectrum shows a peak for iodide at 619 eV, which is mainly attributed to MgI_2, confirming a successful incorporation of iodide into the electrode interphase.

The Ti 2p signal is undetectable in the +10 mM and +20 mM samples but becomes visible in the +40 mM sample, suggesting that the electrode interphase becomes thinner with increasing iodine concentration. In the Mg KLL Auger spectrum, there is no signal at E_K ~1186.6 eV, indicating that metallic Mg cannot be detected. We attribute the absence of metallic Mg signal to the short duration and dynamic nature of potentiodynamic CV plating, which favours fast interphase formation and electrolyte decomposition over sustained bulk metal growth, as previously observed in tests with BF_3·DE.

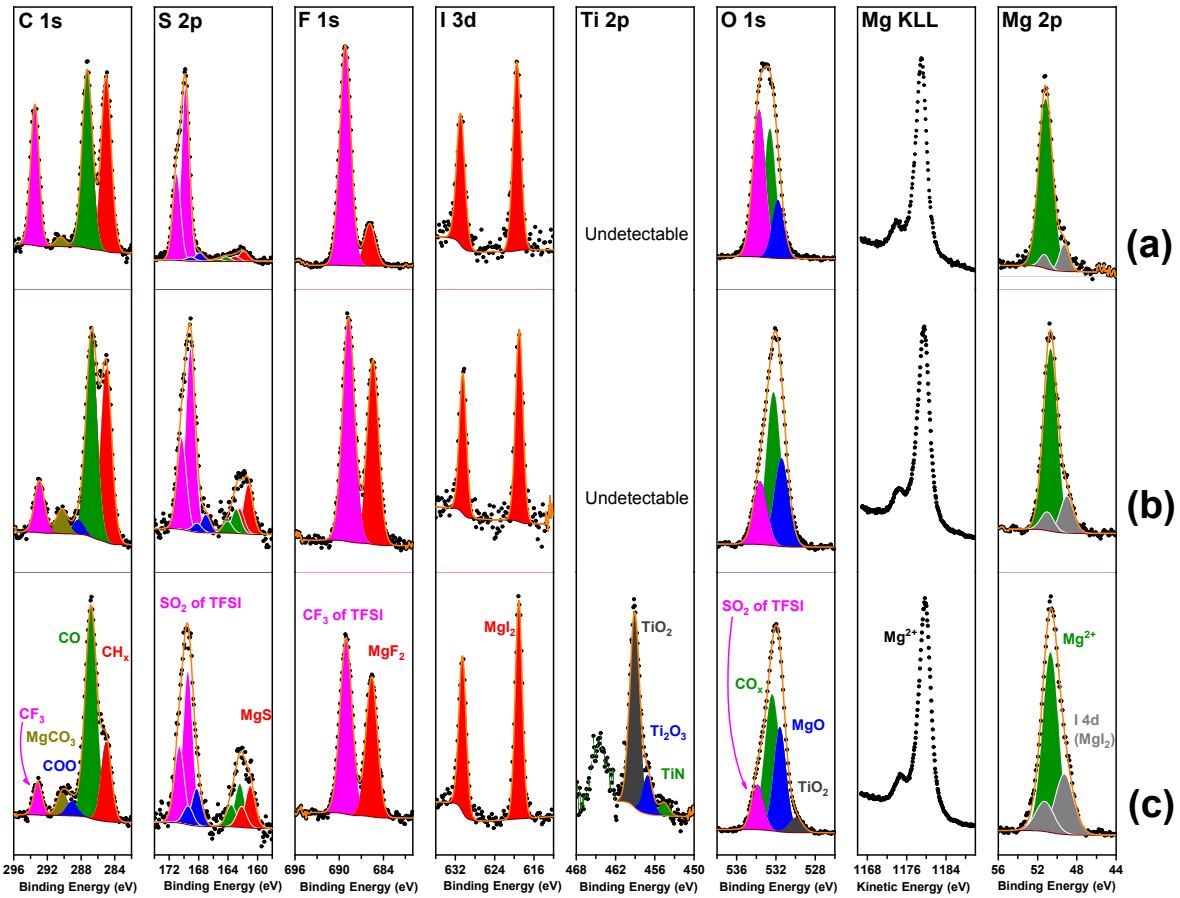

Figure 4: XPS C 1s, S 2p, F 1s, I 3d, Ti 2p, O 1s, Mg 2p and Auger Mg KLL spectra of the electrode interphase formed on Ti electrodes cycled in 0.4 M $Mg(TFSI)_2$ in DME:DG electrolyte with adding (a) 10 mM I_2, (b) 20 mM I_2 and (c) 40 mM I_2 at the end of the 50th plating scan (see Figure 3).

View Article Online
DOI: 10.1039/D6EB00065G

Chart 2 shows that the C–O component increases steadily from 11 at.% (no iodine) to 18, 21, and 26 at.% with the addition of 10, 20, and 40 mM iodine, respectively. Similarly, the amount of MgI_2 increases with more addition of iodine from 0.2 and 0.8 at.% with + 10, + 20 mM I_2 to reach 2 at.% with + 40 mM I_2. Additionally, with more iodine, there is less $Mg(TFSI)_2$ salt in the interphase composition (it decreases significantly from 53 to 25 to 16 at.% with more iodine added). By contrast, the addition of iodine was found not to have significant impact on the MgS and MgF_2 content in the electrode interphase with no clear trend observed (Chart 2), pointing at the presence of iodine not influencing the anion decomposition.

It has been reported that a MgI_2 layer formed on the Mg anode contributes to create a stable, thin, and uniform Mg-ion conductive interphase between the Mg metal and the fluorinated alkoxyborate magnesium electrolyte [21]. DFT calculations further reveal that MgI_2 has a lower vacancy/interstitial formation energy and a very low diffusion barrier for Mg^{2+} compared to MgS, MgF_2, or MgO phases, which promotes high Mg mobility in MgI_2 phases within the interphase [21]. Additionally, MgI_2 is considered a suitable coating material for Mg electrodes because it exhibits reasonable Mg migration barriers (604 ± 160 meV) [18]. Furthermore, it is found that the solvation effect of triiodide I_3^-, formed from the reaction of I^- (in MgI_2) with I_2 in solution, significantly reduces overpotentials for deposition and stripping [22]. In our findings, besides confirming the formation of MgI_2, the addition of iodine results in a much thinner SEI, which may explain the more efficient plating and stripping observed. Thus, the presence of I_2 appears to limit the growth of the interphase.

View Article Online
DOI: 10.1039/D6EB00065G

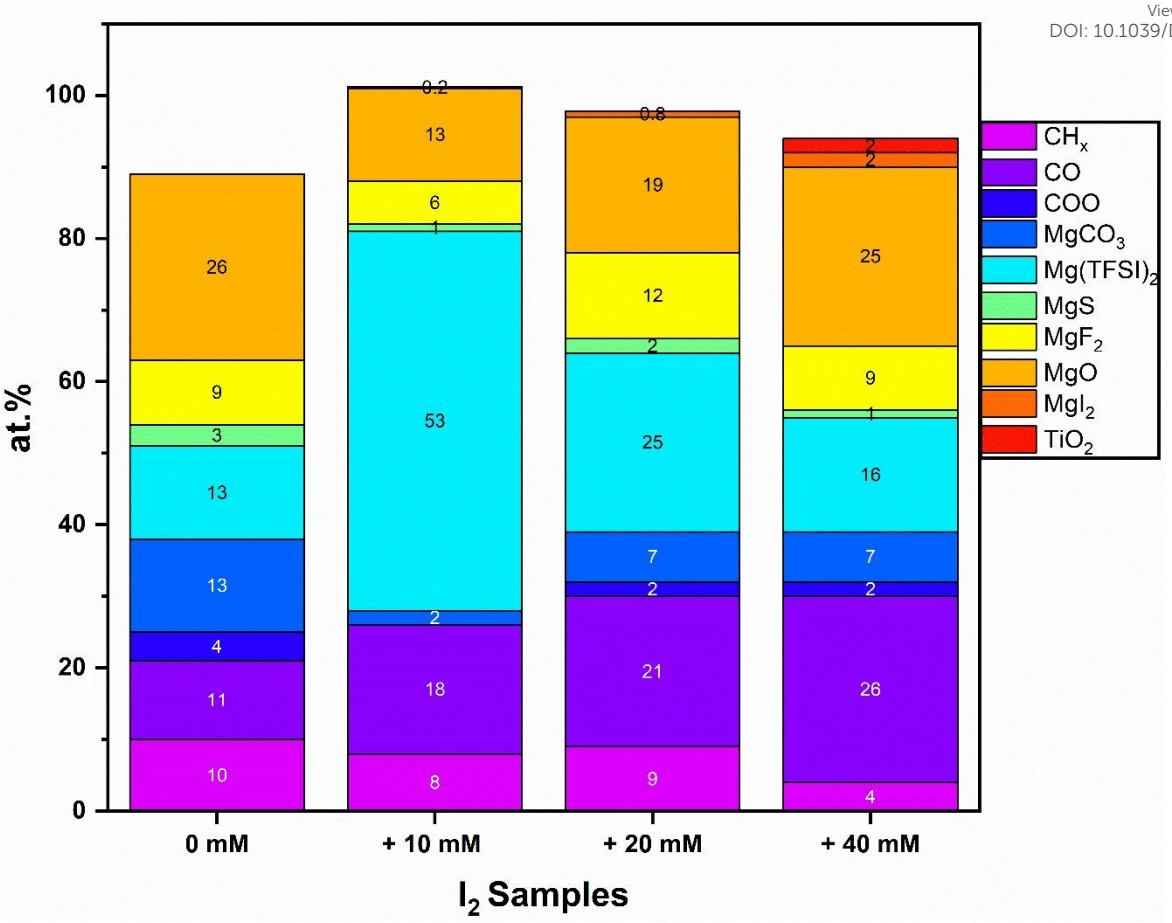

Chart 2: Atomic percentage (at.%) of some of the chemical species observed in XPS spectra reported in Figure 4 and Table S3 (Supporting Information) of the electrode interphase formed on Ti electrodes cycled in 0.4 M $Mg(TFSI)_2$ in DME:DG electrolyte with addition of different concentrations of I_2.

The morphology of the electrodes from the sample with 40 mM I_2 at the end of the 50th plating scan (electrochemical experiment shown in Figure 3 (c) was analyzed using SEM (Figure S4). A relatively smooth deposit with small distributed particles (approximately 1 to 5 µm diameter) is observed on the Ti substrate surface. The overall morphology of the substrate is preserved, which suggests the presence of a thin layer.

Based on the results from using BF_3·DE and I_2 additives to enhance the electrochemistry of magnesium (Mg) plating and stripping, it has been observed that the electrode interphase should ideally:

- Contain boron in both organic and inorganic environments,
- Include the presence of MgI_2,

View Article Online
DOI: 10.1039/D6EB00065G

- Be sufficiently thin to facilitate Mg ion diffusion towards the current collector.

In an attempt to provide both iodide and boron, the use of BI_3 (boron triiodide) additive has been explored. Like BF_3, BI_3 acts as a strong Lewis acid, with the central boron atom being electrophilic because of its empty p orbital. Accordingly, BI_3 is anticipated to react with various nucleophilic species in the electrolyte, including oxygen atoms from solvents or water impurities, particularly given boron's tendency to form strong B–O bonds [23].

c) BI_3 additive

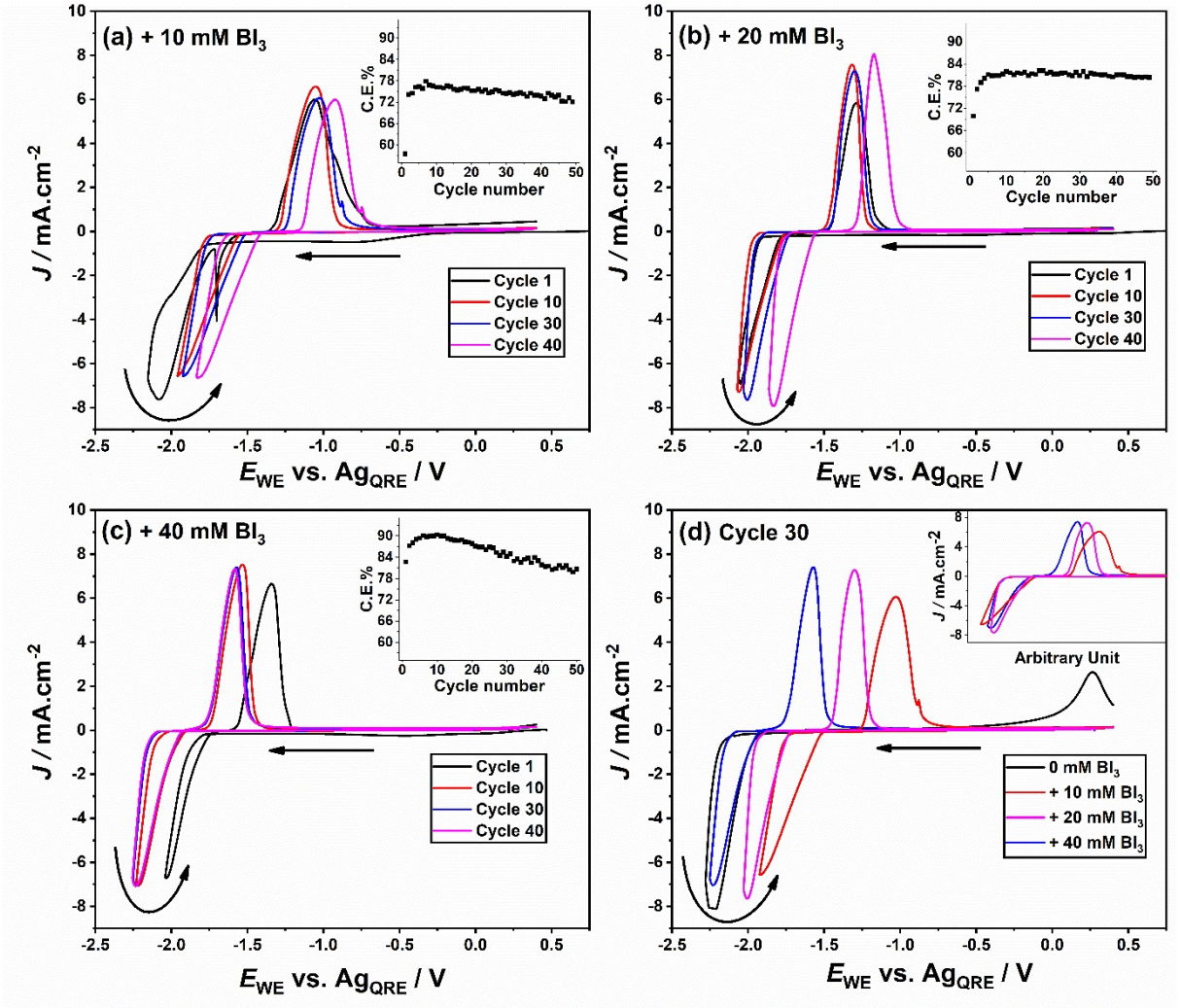

Figure 5: Cyclic voltammograms of a Ti electrode with a scan rate of 25 mV/s at several cycle numbers using 0.4 M $Mg(TFSI)_2$ in DME:DG electrolyte with adding (a) 10 mM, (b) 20 mM, (c) 40 mM of BI_3 and (d) Cyclic voltammograms (30^{th} cycle) of Ti electrodes using 0.4 M

View Article Online
DOI: 10.1039/D6EB00065G

$Mg(TFSI)_2$ electrolyte with a scan rate of 25 mV/s with different amount of BI_3 additive. The insets show the coulombic efficiency over the cycle number.

Figure 5 (a-c) displays the CVs of a 0.4 M $Mg(TFSI)_2$ electrolyte with the addition of 10, 20, 40 mM BI_3 over multiple cycles (1^{st}, 10^{th}, 30^{th}, and 40^{th}). The CVs show a single stripping peak and very low voltage hysteresis between plating and stripping (250-500 mV in the different samples). Stable cycling was also observed after the first cycle. This stability suggests that the addition of BI_3 enhances the electrolyte's performance by stabilising the Mg plating/stripping process. Figure 5 (d) compares the electrochemical performance at the 30^{th} cycle between the electrolyte with and without the BI_3 additive. The presence of BI_3 significantly reduces the voltage hysteresis between plating and stripping, with the peaks' onset potentials difference being approximately 490 mV, 450 mV, and 320 mV with adding 10, 20, 40 mM BI_3. Additionally, the use of BI_3 results in a single stripping peak which becomes narrower as the BI_3 content increases (Figure 5d inset), indicating that BI_3 effectively enhances the kinetics of Mg plating and stripping. In terms of coulombic efficiency (C.E.), the addition of BI_3 leads to noticeable improvements. Indeed, the first cycle C.E. increases from 58 to 82% for BI_3 content from 10 to 40 mM. In all cases, a maximum C.E. is reached after 5-10 cycles with 78, 82 and 90% for 10, 20 and 40 mM BI_3, respectively.

It is important to note that the use of these additives (I_2 and BI_3) influences primarily the stripping peak, with minimal impact on the plating process. This observation suggests that the composition of the electrode interphase plays a more critical role on stripping than plating. Furthermore, the addition of 10 or 20 mM BI_3 proves significantly more effective than the same concentrations of iodine (Figures 3a and 3b), particularly in reducing the voltage hysteresis, improving the stripping kinetics, and enhancing the coulombic efficiency. These findings motivate a closer examination of how BI_3 modifies the electrode interphase composition.

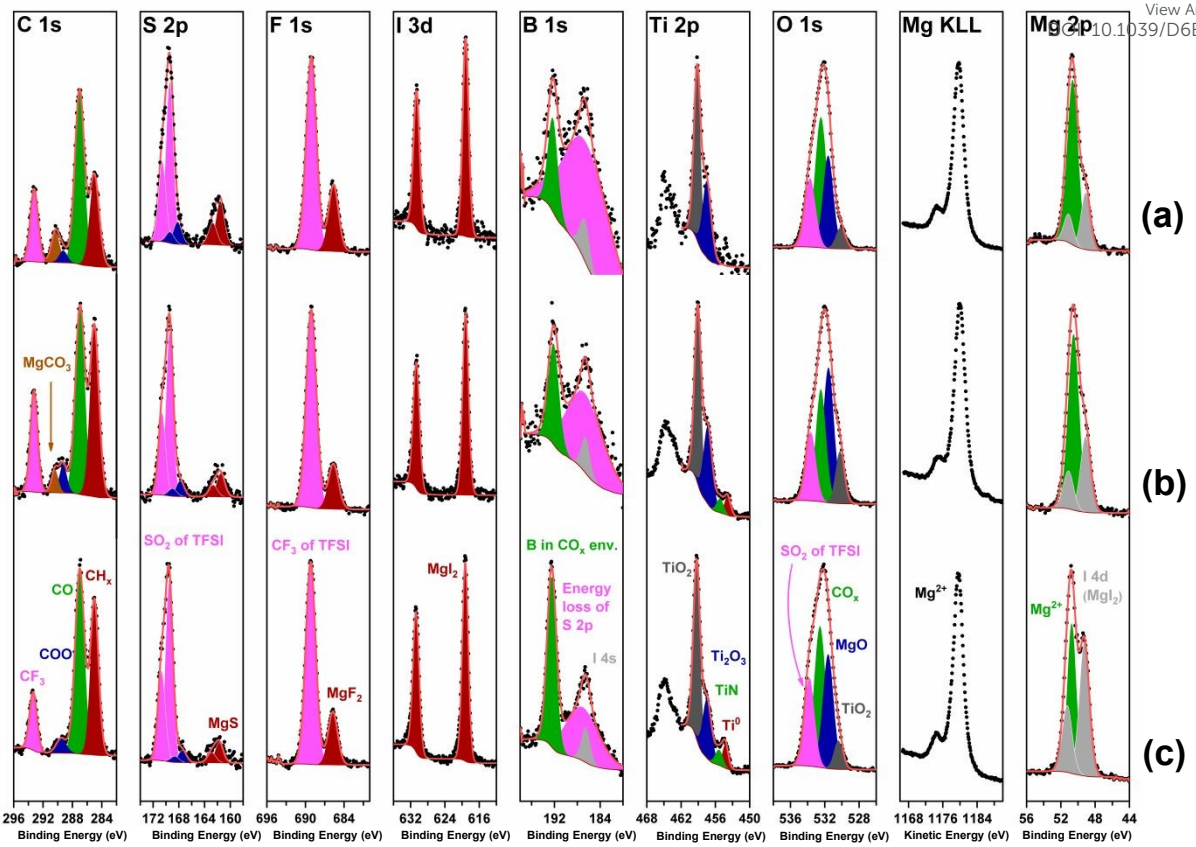

Figure 6: XPS C 1s, S 2p, F 1s, I 3d, B 1s, Ti 2p, O 1s, Mg 2p and Auger Mg KLL spectra of electrode interphase formed on Ti electrodes cycled in 0.4 M $Mg(TFSI)_2$ in DME:DG electrolyte with (a) 10 mM BI_3, (b) 20 mM BI_3 and (c) 40 mM BI_3 at the end of 50th plating scan (see Figure 5).

Figure 6 shows the XPS spectra of a Ti electrode after Mg deposition using a 0.4 M $Mg(TFSI)_2$ electrolyte with 10, 20 and 40 mM BI_3 additive, and the corresponding quantification data are shown in Table S4. The C 1s spectrum reveals peaks corresponding to various carbon species, including hydrocarbons (CH_x), C–O and COO groups, $MgCO_3$ and CF_3 from the TFSI salt. This indicates the presence of organic compounds and degradation products of the electrolyte. Notably, $MgCO_3$ is absent at 40 mM BI_3, suggesting that higher BI_3 concentrations suppress carbonate formation. From S 2p and F 1s spectra, peak associated with MgS and MgF_2 are observed, which indicates the degradation of the TFSI salt. The I 3d spectrum shows peaks consistent with MgI_2, indicating the incorporation of iodide into the anode interphase, originating from the BI_3 additive. The B 1s spectra show three peaks: the broad one represents the energy loos of the S 2p, and a small peak refers to I 4s, while the main peak in green indicates the presence of boron in oxygen environment. However, quantification calculations, similar to

View Article Online
DOI: 10.1039/D6EB00065G

those performed for the BF_3 samples, show that all the oxygen detected in the O 1s spectrum is associated to CO, COO, $MgCO_3$, MgO, TiO_2, and TFSI species. This suggests that the boron from the BI_3 additive has been incorporated into the organic matrix (CO_x) on the electrode surface. The Ti 2p spectra show main peaks corresponding to TiO_2, proving the detection of the Ti substrate. Thus, the presence of BI_3 appears to prevent or at least limit the growth of the electrode interphase, which is very thin (below 5 nm) (or, possibly, incomplete, exposing the underlying TiO_2. Lastly, the Mg KLL and Mg 2p spectra exhibit the typical features observed in the iodine sample (Figure 4), with no significant peak associated with metallic Mg. This suggests that a longer (potentiostatic) deposition is required to detect metallic Mg, as previously observed with the other additives.

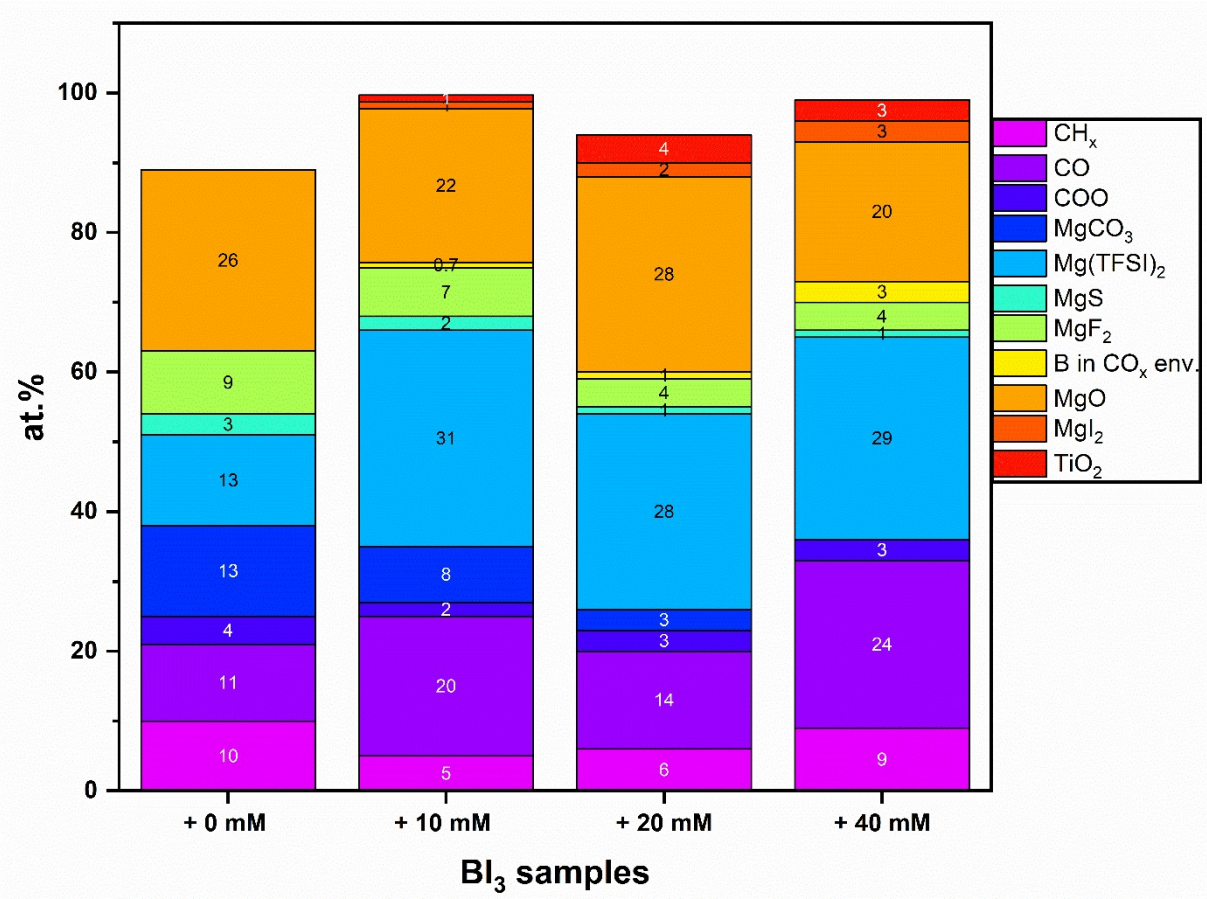

Chart 3: Atomic percentage (at.%) of some of the chemical species observed in XPS spectra reported in Figure 6 and Table S4 of the electrode interphase formed on Ti electrodes cycled in 0.4 M $Mg(TFSI)_2$ in DME:DG electrolyte with addition of different concentrations of BI_3.

View Article Online
DOI: 10.1039/D6EE00065G

Chart 3, derived from the quantitative analysis in Table S4, illustrates clear compositional changes in the electrode interphase with increasing BI_3 concentration. With more additive, there is a progressive enrichment of boron- and iodine-containing species, namely B in CO_x environments and MgI_2, alongside a marked increase in surface $Mg(TFSI)_2$. MgI_2 grows gradually from ~1 at.% at 10 mM to ~3 at.% at 40 mM, while boron incorporation follows a similar trend, rising from ~0.7 to ~3 at.%. The relative proportion of $Mg(TFSI)_2$ nearly doubles compared to the additive-free case (from ~13 to ~28–30 at.%), indicating enhanced salt accumulation or stabilization at the interface under the influence of BI_3.

In contrast, electrolyte degradation products decline with higher BI_3 concentration. $MgCO_3$, initially ~13 at.% without additive, decreases stepwise to ~8 and ~3 at.% at 10 and 20 mM, and disappears entirely at 40 mM. Similarly, MgS diminishes from ~3 to ~1 at.% and MgF_2 decreases from ~9 to ~4 at.%. The suppression of these inorganic decomposition products suggests that BI_3 mitigates parasitic reactions of the electrolyte, thereby limiting uncontrolled interphase growth. Consistent with this, the TiO_2 of the Ti substrate becomes increasingly detectable (from 0 to 3 at.% for increasing BI_3 contents), supporting the interpretation that BI_3 promotes the formation of a thinner electrode interphase.

Overall, these findings suggest that BI_3 modifies the electrode interphase chemistry, favoring a composition rich in the salt residues ($Mg(TFSI)_2$), MgI_2, and B–O_xC more than carbonate, fluoride and sulfide. This change leads to a thinner interphase with higher ionic conductivity, which aligns with the observed lower voltage hysteresis and improved coulombic efficiency and stripping behavior as evidenced in Figure 5. The presence of both boron and iodide in the interphase indicates that BI_3 plays two key roles: (i) iodide and B–O_xC help to limit excessive interphase formation and promote quicker Mg^{2+} transport, and (ii) the strong Lewis acidity of BI_3 removes electrolyte impurities and reactive intermediates and suppresses parasitic reactions.

The morphology of the cycled Ti electrodes was analysed by SEM (Figure S5). In contrast to the relatively smooth deposits observed in the presence of iodine additives (Figure S4), Mg deposition in the BI_3-containing electrolyte results in heterogeneous surface features. The electrode surface is covered by agglomerated spherical structures, often exceeding 10 μm in size, composed of clusters of smaller subparticles with cauliflower-like texture. In some regions, flower-like crystallites with radially arranged structures are also observed. Toward the central region of the electrode, the deposits appear mainly as isolated spherical particles

View Article Online
DOI: 10.1039/D5EB00065G

exhibiting a highly porous and interconnected morphology. Despite the relatively high deposition current reached during the potentiostatic step, no dendritic structures were detected, indicating that Mg growth proceeds through agglomerated and porous particle formation under these conditions.

Among all of the additives, 40 mM BI_3 shows the best electrochemical performance in terms of cyclability, coulombic efficiency and voltage hysteresis as summarized in Table 1. Thus, it has been chosen to check its compatibility with various current collectors and with the Mo_6S_8 Chevrel phase as the positive electrode.

To evaluate the electrochemical stability of the 0.4M $Mg(TFSI)_2$ + 40 mM BI_3 electrolyte and its compatibility with various current collectors (SS, Ti, and Al substrates), linear sweep voltammetry (LSV) experiments were performed at a scan rate of 0.1 mV/s. The measurements were conducted using both Ag and Mg reference electrodes to assess stability in different potential windows relevant to Mg battery operation. As shown in Figure 7(a), LSV curves recorded *vs.* Mg reference electrode demonstrate that Ti exhibits a significantly higher oxidative stability limit (~3.0 V *vs.* Mg^{2+}/Mg) compared to SS (~2.2 V *vs.* Mg^{2+}/Mg). Additionally, open-circuit potential (OCP) measurements performed immediately after immersion of each substrate in the electrolyte (prior to LSV) revealed a notable potential drop of approximately 0.8 V for the Al foil (Supplementary Figure S6b), indicating a possible chemical interaction upon immersion or modification of interfacial properties (possible formation of AlI_3) when in contact with the electrolyte. This suggests limited suitability of Al as a stable current collector in the 0.4M $Mg(TFSI)_2$ + 40 mM BI_3 electrolyte.

Table 1: Comparative Comparison of 0.4 M $Mg(TFSI)_2$ electrolytes without and with using additives (BF_3·DE, I_2, BI_3) in terms of voltage hysteresis, Coulombic efficiency and Interphase chemistry.

Electrolyte		**Voltage Hysteresis (V.H.)**	**Coulombic Efficiency (C.E.)**	**Interphase Chemistry / Features**[1]	**Notes**
0.4 M $Mg(TFSI)_2$	**(no additive)** [5]	>2000 mV	<60% Decreasing over cycling	Thick (>5 nm), resistive interphase, carbonate/sulfide/fluoride accumulation	Poor reversibility
+ BF_3	**1.5 wt.%**	500-1400 mV (oxidation peak A)	<60%	Thick (>5 nm), rich with MgF_2, suppressed $MgCO_3$	Poor reversibility but with

[1] The thickness is based on the probing depth of the Ti 2p

	4 wt.%	450-600 mV (oxidation peak A)	<30%		lower V.H. *vs.* no additive
	8 wt.%	450-600 mV (oxidation peak A)			
+ I_2	**10 mM**	500-680 mV (oxidation peak A)	<65% Decreasing over cycling	Thick (>5 nm),	40 mM shows significant improvement in V.H. and C.E. *vs.* no additive
	20 mM	400-650 mV (oxidation peak A)			
	40 mM	~350 mV	~70% first cycle; stabilizes at ~83% (cycle 30)	thin (<5 nm), MgI_2–rich interphase with less carbonate/sulfides/fluorides	
+ BI_3	**10 mM**	450–500 mV	Peak ~78%, then gradually decreases to 72%	Thin (<5 nm), $Mg(TFSI)_2$-rich interphase + including (MgI_2, B–CO_x); suppressed $MgCO_3$, MgS, MgF_2 with more additives	Lewis acidity of BI_3 aids impurity scavenging
	20 mM	450-480 mV	Increase and stabilizes ~82% after 20 cycles.		
	40 mM	250–350 mV	Peak ~89% (cycle 10); ~80% after 40 cycles		

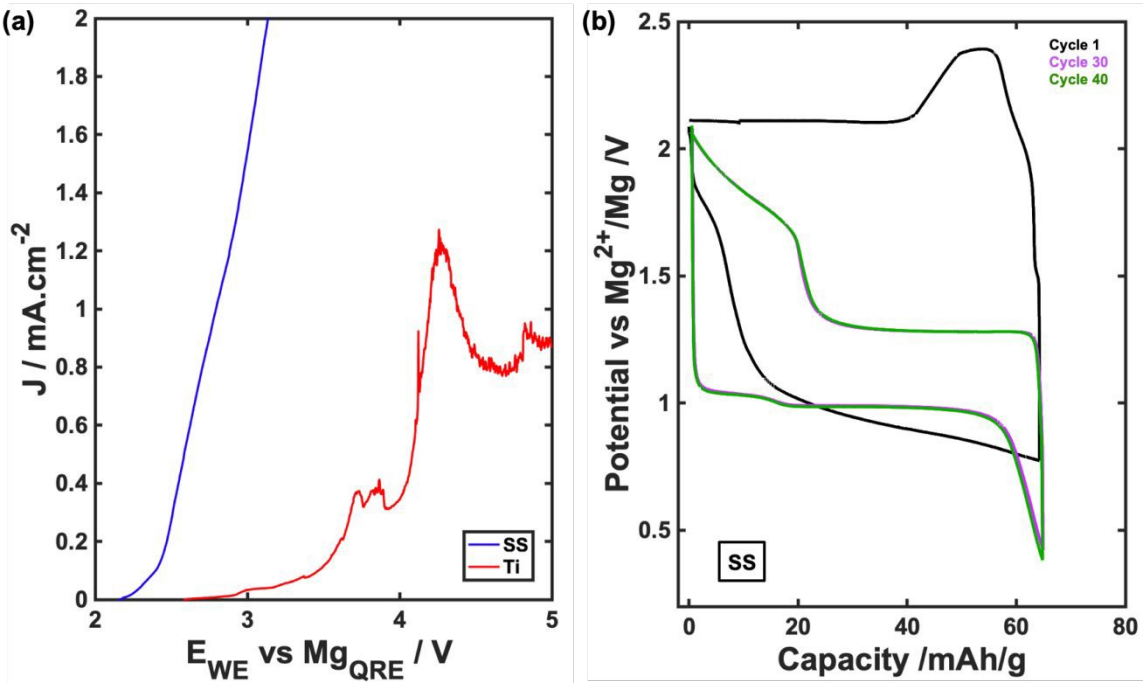

Figure 7: (a) LSV of SS and Ti electrodes with a scan rate of 0.1 mV/s using 0.4 M $Mg(TFSI)_2$ in DME:DG electrolyte with 40 mM of BI_3 *vs.* Mg_{QRE}. (b) Galvanostatic cycling with potential limitation (GCPL) at C/10 of Chevrel phase positive electrode casted on SS

foil, using 0.4 M $Mg(TFSI)_2$ in DME:DG with 40 mM BI_3, in a 2-electrode Swagelok cell and a Mg disk negative electrode. Typical potential profiles are displayed for various cycle.

Following the anodic stability studies, the compatibility of the 0.4M $Mg(TFSI)_2$ + 40 mM BI_3 electrolyte with the Mo_6S_8 Chevrel phase positive electrode was assessed. Although not used in commercial products due to energy density limitations, Chevrel phases are widely used as a benchmark positive electrode in Mg battery research, especially for evaluating and optimizing new electrolyte formulations. Indeed, Mo_6S_8 is chemically stable during cycling and across various voltages, making it reliable for isolating electrolyte effects from material degradation. The electrochemical performance of Mo_6S_8 positive electrode, cast on SS and Ti substrates, was investigated in 2-electrode Swagelok cells with Mg metal as the negative/counter electrode. The galvanostatic cycling performance of Mo_6S_8 on SS is presented in Figure 7(b), highlighting the activation overpotential in the first cycle (likely due to interfacial Mg stripping/plating overpotential) and the emergence of typical highly stable voltage profiles with discharge plateau around 1.0 V *vs.* Mg^{2+}/Mg, illustrated for cycles 30 and 40. The full cycling data, displayed in Supplementary Figure S7(a), confirm cycling stability and full capacity retention corresponding to the reversible insertion/deinsertion of ~1 Mg^{2+} per formula unit. In contrast, despite the higher anodic stability of Ti observed in LSV, the Mo_6S_8 positive electrode cast on Ti foil displayed poor cyclability, retaining acceptable performance only over the first 5–6 cycles (Supplementary Figure S7(b). Post-mortem observations suggest that this rapid degradation potentially stems from poor adhesion between the active layer and the Ti substrate, leading to progressive loss of electrical contact during cycling. Mo_6S_8 electrodes cast on Al foil showed even worse stability, failing to sustain more than three cycles, likely due to chemical instability of the substrate in this electrolyte as discussed previously. These results are summarized and compared in Table 2.

Table 2: Electrochemical stability and cycling performance of stainless steel (SS), titanium (Ti), and aluminum (Al) current collectors in 0.4 M $Mg(TFSI)_2$ + 40 mM BI_3 electrolyte with the Mo_6S_8 Chevrel phase positive electrode

Substrate	Anodic Stability (vs Mg^{2+}/Mg)	OCP Behavior	Mo_6S_8 Cycling	Limiting Factor

Stainless steel (SS)	~2.5 V	Stable	Long-term stable, full capacity retention (~1 Mg^{2+}/formula unit.)	Moderate oxidative stability, but acceptable
Titanium (Ti)	~3.5 V	Stable	Fades after 5–6 cycles	Poor adhesion/contact loss
Aluminum (Al)	Unstable (OCP drop ~0.8 V, likely AlI_3 formation)	Chemically unstable	-----	Substrate–electrolyte reactivity

The comparison in Table 3 highlights that the BI_3 additive substantially improves $Mg(TFSI)_2$ electrolytes performance by significantly reducing the voltage hysteresis, stabilising coulombic efficiency, and altering interphase chemistry toward thinner, salt-rich, and more conductive layers. On stainless steel, the electrolyte supports long-term stable cycling of Mo_6S_8, while titanium, despite its superior anodic stability (~3.5 V vs. Mg), suffers from adhesion problems, leading to rapid performance degradation.

When benchmarked against state-of-the-art $Mg[B(HFIP)_4]_2$ electrolytes[14,24–26], the BI_3 system shows impactful improvements relative to additive-free $Mg(TFSI)_2$ but still lags in terms of long-term coulombic efficiency (>90%) and overpotential (<200 mV). $Mg[B(HFIP)_4]_2$ electrolytes also offer superior oxidative stability which enables to operate with higher-voltage positive electrodes. However, their complex synthesis, moisture sensitivity, and high cost limit large-scale practicality. In contrast, BI_3 additive represents a simpler, scalable strategy that effectively suppresses parasitic reactions and tailors the interphase chemistry.

Table 3: Comparative Comparison 0.4 M $Mg(TFSI)_2$ + 40 mM BI_3 electrolyte against state-of-the-art $Mg[B(HFIP)_4]_2$ systems in terms of voltage hysteresis, coulombic efficiency, interphase chemistry, and oxidative stability.

Electrolyte	Voltage Hysteresis	Coulombic Efficiency	Interphase Chemistry	Oxidative Stability	Notes
0.4 M $Mg(TFSI)_2$ (no additive) [5]	>2000 mV	<60%	Thick, resistive interphase, carbonate/sulfide accumulation	~3.5 V (Ti);	Poor reversibility
0.4 M $Mg(TFSI)_2$ + 40 mM BI_3	250–350 mV	~89% peak (cycle 10), ~80% after 40 cycles	Thin, the layer rich with the salt, MgI_2 and B–CO_x; suppressed $MgCO_3$, MgS, MgF_2	~3.0 V on Ti (but cathode adhesion issues); 2.2 V (SS)	Simple additive approach based on commercial salts
$Mg[B(HFIP)_4]_2$[14,24–26]	Typically, <200 mV	>90% (often 95–	Ionically conductive; boron-containing surface	~4.0 V on SS,	State-of-the-art.

View Article Online
DOI: 10.1039/D6EB00065G

		99%) over extended cycles	layers with minimal parasitic products	enabling high-voltage cathodes	Moisture-sensitive, costly, complex synthesis

4) Conclusion and outlook

In this study, we have explored the impact of various electrolyte additives, namely boron trifluoride diethyl etherate ($BF_3{\cdot}O(C_2H_5)_2$), iodine (I_2), and boron triiodide (BI_3), on the kinetics of magnesium plating and stripping, voltage hysteresis, and coulombic efficiency. This comprehensive analysis reveals how these additives influence the composition of the electrode interphase and their overall electrochemical performance. Our findings indicate that an ideal electrode interphase should be thin (<5 nm) and contain both iodide and boron. The addition of 40 Mm of BI_3 to 0.4 M $Mg(TFSI)_2$/DME:DG effectively achieves this and participates in improving coulombic efficiency (90-80%), voltage hysteresis (250-350 mV) and the kinetic of magnesium plating and stripping.

Electrochemical results with Mo_6S_8 electrodes highlight the importance of the current collector used, impacting not only the electrochemical stability (corrosion) but also on interfacial and mechanical compatibility. Despite Ti's higher anodic stability, its poor adhesion with the Chevrel phase composite electrode leads to rapid capacity fade, likely due to contact loss during cycling. In contrast, SS supports stable cycling with full capacity retention, suggesting more favourable interfacial properties. Overall, substrate selection must account for both the electrochemical window and interface stability.

While $Mg[B(HFIP)_4]_2$ still offers lower overpotentials, higher oxidative stability and coulombic efficiency, its costly complex synthesis, and moisture sensitivity limit its applicability. Thus, $Mg(TFSI)_2$ + BI_3 is an interesting alternative for routine material testing purposes. More importantly, two promising SEI components have been identified (MgI_2 and $B–O_xC$), and the role of impurity scavenger of strong Lewis acid additive such as BI_3 has been highlighted, enabling to suppression of the formation of detrimental electrode interphase components such as fluorides, sulfides and/or carbonates. We foresee that this additive will become extremely useful in the development of future Mg-based electrolytes, as it should provide advantageous SEI engineering features as well as impurity scavenging properties. This latter aspect can

View Article Online
DOI: 10.1039/D6EB00065G

significantly lower future Mg cell production cost by lowering the requirements on electrolyte purification procedures and making the Mg-based electrolytes less air sensitive.

Conflicts of interest

There are no conflicts of interest to declare.

Data availability

The data supporting the findings of this study are available within the article and its Supplementary Information. Any Additional data of this study are available from the corresponding author upon reasonable request.

Acknowledgements

R.D. thanks the French National Research Agency (STORE-EX Labex Project ANR-10-LABX-76-01) for financial support. A.P. gratefully acknowledges funding from the European Research Council (ERC) under the European Union's Horizon 2020 research and innovation programme (grant agreement no. 101089281) and the Spanish Agencia Estatal de Investigación Severo Ochoa Programme for Centres of Excellence in R&D (CEX2023-001263-S). M.R. acknowledges the European Union H2020-MSCA-COFUND Program for grant #945357 (DESTINY project) cofunded by the University of Pau & Pays Adour.

References

1 H. Zhang, L. Qiao and M. Armand, *Angew. Chem.*, 2022, **61**, e202214054.

2 R. Mohtadi and F. Mizuno, *Beilstein Journal of Nanotechnology*, 2014, **5**, 1291–1311.

3 S. Y. Ha, Y. W. Lee, S. W. Woo, B. Koo, J. S. Kim, J. Cho, K. T. Lee and N. S. Choi, *ACS Appl. Mater. Interfaces*, 2014, **6**, 4063–4073.

4 I. Shterenberg, M. Salama, H. D. Yoo, Y. Gofer, J.-B. Park, Y.-K. Sun and D. Aurbach, *J. Electrochem. Soc.*, 2015, **162**, A7118–A7128.

5 M. Radi, T. Purkait, D. S. Tchitchekova, A. R. Goñi, R. Markowski, C. Bodin, C. Courrèges, R. Dedryvère and A. Ponrouch, *Adv. Energy Mater.*, 2024, 2401587.

6 J. G. Connell, B. Genorio, P. P. Lopes, D. Strmcnik, V. R. Stamenkovic and N. M. Markovic, *Chemistry of Materials*, 2016, **28**, 8268–8277.

7 S. J. Kang, H. Kim, S. Hwang, M. Jo, M. Jang, C. Park, S. T. Hong and H. Lee, *ACS Appl. Mater. Interfaces*, 2019, **11**, 517–524.

8 F. Sagane, K. Ogi, A. Konno, M. Egashira and K. Kanamura, *Electrochemistry*, 2016, **84**, 76–78.

9 F. Sagane, K. Ogi, A. Konno and K. Kanamura, *J. Electrochem. Soc.*, 2021, **168**, 120528.

10 W. Wang, S. Ju, H. Zhang, X. Zhou and X. Yu, *Energy Storage Mater.*, 2024, **70**, 103493.

11 H. Wang, X. Feng, Y. Chen, Y. S. Liu, K. S. Han, M. Zhou, M. H. Engelhard, V. Murugesan, R. S. Assary, T. L. Liu, W. Henderson, Z. Nie, M. Gu, J. Xiao, C. Wang, K. Persson, D. Mei, J. G. Zhang, K. T. Mueller, J. Guo, K. Zavadil, Y. Shao and J. Liu, *ACS Energy Lett.*, 2020, **5**, 200–206.

12 J. D. Forero-Saboya, D. S. Tchitchekova, P. Johansson, M. R. Palacín and A. Ponrouch, *Adv. Mater. Interfaces*, 2022, **9**, 2101578.

13 X. Li, T. Gao, F. Han, Z. Ma, X. Fan, S. Hou, N. Eidson, W. Li and C. Wang, *Adv. Energy Mater.*, 2017, **8**, 1701728.

14 T. Pavčnik, M. Radi, O. Lužanin, R. Dedryvère, D. S. Tchitchekova, A. Ponrouch, J. Bitenc and R. Dominko, *J. Power Sources*, 2025, **626**, 235711.

15 J. Forero-Saboya, C. Bodin and A. Ponrouch, *Electrochem. commun.*, 2021, **124**, 106936.

16 M. Radi, N. Ibadulla, C. Courrèges, A. Ponrouch and R. Dedryvère, *Batter. Supercaps*, 2025, e202500177.

17 B. Li, R. Masse, C. Liu, Y. Hu, W. Li, G. Zhang and G. Cao, *Energy Storage Mater.*, 2019, **22**, 96–104.

18 T. Chen, G. Sai Gautam and P. Canepa, *Chemistry of Materials*, 2019, **31**, 8087–8099.

19 X. Huang, S. Tan, J. Chen, Z. Que, R. Deng, J. Long, F. Xiong, G. Huang, X. Zhou, L. Li, J. Wang, L. Mai and F. Pan, *Adv. Funct. Mater.*, 2024, **34**, 2314146.

20 C. Bodin, J. Forero Saboya, P. Jankowski, K. Radan, D. Foix, C. Courrèges, I. Yousef, R. Dedryvère, C. Davoisne, M. Lozinšek and A. Ponrouch, *Batter. Supercaps*, 2023, **6**, e202200433.

21 V. Bhaghavathi Parambath, Z. Zhao-Karger, T. Diemant, M. Jäckle, Z. Li, T. Scherer, A. Gross, R. J. Behm and M. Fichtner, *J. Mater. Chem. A Mater.*, 2020, **8**, 22998–23010.

22 N. Z. Hardin, C. P. Woodley, K. D. McDonald and B. M. Bartlett, *ACS Appl. Mater. Interfaces*, 2024, **16**, 14883–14889.

23 J. Clayden, N. Greeves and S. Warren, *Organic Chemistry*, Oxford University Press Inc., second edition., 2012.

24 Z. Zhao-Karger, R. Liu, W. Dai, Z. Li, T. Diemant, B. P. Vinayan, C. Bonatto Minella, X. Yu, A. Manthiram, R. J. Behm, M. Ruben and M. Fichtner, *ACS Energy Lett.*, 2018, **3**, 2005–2013.

25 Z. Zhao-Karger, M. E. Gil Bardaji, O. Fuhr and M. Fichtner, *J. Mater. Chem. A Mater.* 2017, **5**, 10815–10820.

26 J. Luo, Y. Bi, L. Zhang, X. Zhang and T. L. Liu, *Angewandte Chemie International Edition*, 2019, **58**, 6967–6971.

View Article Online
DOI: 10.1039/D6EB00065G

View Article Online
DOI: 10.1039/D6EB00065G

Data availability

The data supporting the findings of this study are available within the article and its Supplementary Information. Any Additional data of this study are available from the corresponding author upon reasonable request.